



Analysis and modeling of cycle aging of a commercial LiFePO₄/graphite cell

Maik Naumann^{*}, Franz B. Spingler, Andreas Jossen

Institute for Electrical Energy Storage Technology (EES), Technical University of Munich (TUM), Arcisstraße 21, 80333, Munich, Germany

HIGHLIGHTS

- First cycle aging study for widely commercially used LFP/graphite cell from Sony.
- Experiments by 19 cycle aging and 17 calendar aging test points over 885 days.
- Analysis of cycle aging influence of temperature, C-rate, DOC and SOC-range.
- Semi-empirical model for cycle aging estimation of cell capacity and resistance.
- Model validation with further dynamic aging study based on 2 application profiles.

ARTICLE INFO

Keywords:

Lithium-ion battery
LiFePO₄
(LFP)/Graphite
Cycle aging
Lifetime model
Dynamic cycle conditions

ABSTRACT

This paper presents cycle aging results of a commercial lithium-ion cell from a comprehensive, 29 month aging study and follows up on calendar aging results published previously [1]. We use a widely used commercial LiFePO₄/graphite cell from *Sony/Murata*, which promises long calendar and cycle lifetime, that would make it suitable for stationary battery applications. The evolution of the cells' capacity and impedance are shown in a static cycle aging study for 19 test points with different combinations of temperature, C-rate, depth of discharge and state of charge. Based on the measurement data shown herein and the calendar aging model presented in the previous paper, a semi-empirical combined aging model is presented for the capacity loss and resistance increase. Two dynamic load profiles are used to experimentally validate the combined aging model. Absolute model errors below 1% for the capacity loss and below 2% for the resistance increase in both dynamic load profiles demonstrate that the combined aging model can predict the lifetime of LiFePO₄/graphite battery cells for different applications and varying operation conditions adequately. In the cycle experiments, an unexpectedly strong, but partly reversible capacity loss is observed with shallow cycles at medium states of charge.

1. Introduction

1.1. Motivation

This paper presents the results of a comprehensive cycle aging study spanning 885 days of experiments, which is used to develop an aging model enabling battery lifetime predictions as a function of the cycling conditions temperature, C-rate, (DOC), and (SOC). All experiments are performed with a commercial *Sony/Murata* 3Ah 26650 LFP/C cell (see Section 2.1). This cycle aging study was part of an extended aging study [2] with an additionally performed calendar aging study based on the same cell [1].

This cell, branded as *fortelion*, is used in many commercial home energy storage systems. The cell was also deployed in the 192 kWh *Energy Neighbor* battery energy storage system in container format [3,4], which was developed in the project *EEBatt* [5].

1.2. Literature review

Cycle aging occurs during charging and discharging of a battery. Similar to calendar aging, cycle aging leads to loss of lithium inventory (LI), loss of active material (LAM) and the increase of the impedance [6]. With a commercial LFP/C cell, Li et al. [7] observed accelerated growth of the solid electrolyte interphase (SEI) during cycling at room

^{*} Corresponding author.

E-mail address: maik.naumann@tum.de (M. Naumann).

URL: <http://www.ees.ei.tum.de/en/> (M. Naumann).

<https://doi.org/10.1016/j.jpowsour.2019.227666>

Received 12 September 2019; Received in revised form 2 December 2019; Accepted 26 December 2019

Available online 25 January 2020

0378-7753/© 2020 Elsevier B.V. All rights reserved.

Table 1

Selected literature on lithium-ion battery cycle aging modeling by model and cell types.

Aging model type	LFP/C	Other cell types
None (tests only)		[8,15–17]
Empirical	[9,13,18]	
Semi-empirical	[19,20]	[10,11,21]
Physico-chemical	[12,22–25]	

temperature and an additional blocking mechanism of graphene layers on the anode solid electrolyte interphase (SEI) during cycling at 60°C. It was demonstrated that the LAM on the anode is caused mainly by Fe that dissolves from the cathode and is deposited on the graphite surface during cycling. Cycling alters the surface areas of the anode: The lithiation and delithiation in the active material of the electrodes lead to a volume expansion and possible fracturing of the electrodes. This is not the case during storage. Hence, different SEI surfaces with individual areas and growth speed emerge. Additionally to SEI growth and wear of active mass, lithium plating can occur at low temperatures and/or high currents leading to accelerated aging [8].

In cycle aging experiments, the effects of cycle aging are usually superposed with those of calendar aging. Hence, to obtain the pure cycle aging effects, the calendar aging effects have to be estimated and subtracted from the total aging. The pure cycle aging correlates with the charge and discharge throughput in Ah or full equivalent cycle (FEC). Important influence factors on cycle aging are the cell's temperature, C-rate, DOC and the SOC-range [9].

Table 1 shows a selection of different cycle aging studies. Various types of models have been applied to simulate aging behavior: Empirical, Semi-empirical and Physico-chemical. Most of the cycle aging studies investigate the influence of temperature and C-rate and some studies investigate the influence of DOC and SOC-range. Only Lepiorz [9] (LFP/C cells) and de Hoog et al. [10] (NMC/C cells) consider all four influence factors on cycle aging in their experiments. Lepiorz tested various combinations of SOC and DOC [9] but the proposed aging model considers only temperature and C-rate. Furthermore, this aging model was not validated with dynamic profiles with varying influence factors. Only some of the presented studies tested their aging models with dynamic profiles [10–14].

It can be concluded that various studies have investigated specific aging effects relevant to LFP/C cycle aging but the validity of the models proposed so far has been limited. In this work we develop a cycle aging model based on a long term experiment with numerous cycle aging conditions for temperature, C-rate, DOC and SOC-range. The aging model is then validated systematically with dynamic load profiles.

1.3. Paper highlights

In this paper we present a comprehensive cycle aging study for a widely commercially used LFP/C cell (see Section 2.1). A total of 19 test points (TPs) is investigated in a static cycle aging study, using three cells per TP. Various temperatures, C-rates, DOCs, SOC are investigated over a period of 885 days. Two dynamic battery stress profiles are examined in a dynamic cycle aging study, with alternating conditions of C-rates, DOC and SOC. The experimental data is analyzed and a semi-empirical aging model is proposed that combines calendar aging and cycle aging. The dynamic stress profiles used in the aging experiment are used to validate the aging model.

1.4. Paper structure

First, the experimental setup and the measurement methods of the cycle aging study are described in Section 2. In Section 3 the aging data is presented and verified. Then, a semi-empirical cycle aging model is derived and validated with the data from the dynamic cycle aging study test points (TPs). The results of the cycle aging study, the aging model development, and the model validation using dynamic cycle profiles are summarized in Section 4. Section 5 provides an outlook of ongoing investigations on the DOC-influence of the cycle aging and the development of enhanced aging models.

2. Experimental

In this section, the investigated cell and the measurement procedures will be discussed, followed by a description of the overall testing procedures. Finally, the design of experiments for both the static cycle aging study and the dynamic validation profiles are described.

2.1. Investigated cell

Commercially available Sony/Murata US26650FTC1 26650 LFP/C cells are investigated. Table 2 shows the most important cell parameter values from the manufacturer's datasheet. The cells' rated capacity is 2.85Ah. However, in a previous characterization of over 1100 cells from two batches [26], the mean discharge capacity was 3.019Ah at a constant current discharge of 3.0A and a CV-phase (CV at 2.0 V until $I_{\text{disch,CV}} < C/20 = 150 \text{ mA}$) after charging at a constant current of 3.0A and a CV-phase (CV at 3.6 V until $I_{\text{ch,CV}} < C/30 = 100 \text{ mA}$). Consequently, C-rates in this study are based on a capacity of 3.0 Ah.

2.2. Measurement equipment

The capacity measurements (CMs) were performed with two BaSyTec BaSyTec cell test systems (CTSs), each with 32 channels, and an

Table 2

Datasheet values of the investigated LiFePO₄/graphite cell Sony US26650FTC1.

Parameter	Value	Notes
Nominal capacity	2.850Ah	Datasheet capacity
Nominal voltage	3.000Ah	Measured cell capacity in this study
Max. charge voltage	3.2 V	
Min. discharge voltage	3.65 V	Datasheet definition
Ohmic impedance (1 kHz), AC	3.6 V	Voltage applied in this study
Max. continuous charge current	2.00 V	
Max. continuous discharge current	18 mΩ	Datasheet definition
Temperature range charge	2.85A	Current applied in this study
Temperature range discharge	3.00A	
Mass	20A	Datasheet: Max. surface temperature 60°C
	0°C to 45°C	Datasheet: Max. surface temperature 80°C
	–20°C to 60°C	
	84.5 g	

Espec LU-123 climate chamber at $T = 25^\circ\text{C}$. The surface temperature of each cell was monitored using NTC thermistors. Electrochemical impedance spectroscopy (EIS) measurements were performed with a BioLogic VMP3 potentiostat with 16 channels and a climate chamber at $T = 25^\circ\text{C}$.

2.3. Measurement procedures

Two different measurement procedures were applied: Standard check-up (CU) and extended CU. The standard CU consists of a CM and is followed by an electrochemical impedance spectroscopy (EIS) measurement, which are not evaluated in this paper. The extended CU is principally the same as the standard CU, but between the CM and EIS, a low rate charge and discharge at $I_{ch/dis,CC} = C/50$ is performed. Both procedures involve the following CM test plan at 25°C :

1. Initial discharge: CCCV protocol to 2.0 V using a constant-current (CC) $I_{dis,CC} = 1C = 3\text{ A}$ followed by a CV-phase until $I_{dis,CV} < C/20 = 150\text{ mA}$. 25min relaxation pause.
2. Two consecutive full cycles: Full charge: CCCV protocol to 3.6 V using a CC $I_{ch,CC} = 1C = 3\text{ A}$ followed by a CV until $I_{ch,CV} < C/30 = 100\text{ mA}$. 25 min relaxation pause. Full discharge: CCCV protocol to 2.0 V using a CC $I_{dis,CC} = 1C = 3\text{ A}$ followed by a CV-phase until $I_{dis,CV} < C/20 = 150\text{ mA}$. 25 min relaxation pause.
3. SOC adjustment: Charging with $I_{ch,CC} = 1C = 3\text{ A}$ until reaching 50% SOC based on the mean value of the actual capacity measured in the two full discharge steps. 25 min relaxation pause.
4. Pulses: 1/3C discharge pulse for 10s, 10min relaxation, 1/3C charge pulse. 10min relaxation. Then the same pulse procedure is applied again with 2/3C and 1C.

In this CM, the capacity is determined by performing two consecutive full cycles in order to minimize the influence of the possible recovery effect due to the anode overhang [27]. Furthermore, both full cycles are performed with CV-phases in the charge and also in the discharge direction aiming to obtain all the available capacity. The discharge CV-phases last on average 285 s for the first cycle and 272 s for the second cycle resulting in about 2.4% and 2.2% of the total capacity at

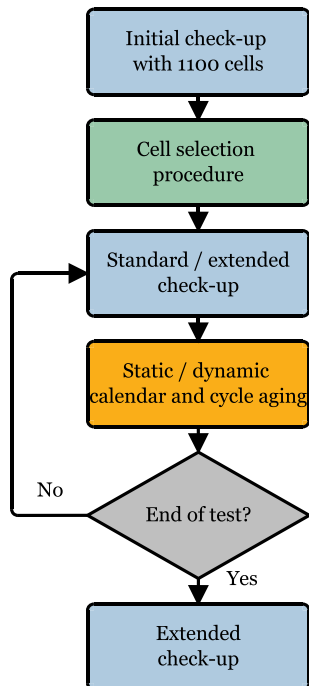


Fig. 1. Testing procedure of the cycle aging study.

Table 3

Test matrix of the static cycle aging study with three cells for each test point. The test points marked with * were started later during the course of the static cycle aging study.

Test point	Temperature	DOC	Average	Charge	Discharge	CV-phase
			SOC	C-rate	C-rate	
TP1*	25°C	100%	50%	1.0C	1.0C	Charge
TP2	25°C	80%	50%	1.0C	1.0C	None
TP3*	25°C	20%	50%	1.0C	1.0C	None
TP4	40°C	100%	50%	1.0C	1.0C	Charge
TP5	40°C	100%	50%	1.0C	1.0C	None
TP6	40°C	80%	50%	1.0C	1.0C	None
TP7	40°C	40%	50%	1.0C	1.0C	None
TP8	40°C	20%	50%	1.0C	1.0C	None
TP9	40°C	10%	50%	1.0C	1.0C	None
TP10	40°C	5%	50%	1.0C	1.0C	None
TP11*	40°C	1%	50%	1.0C	1.0C	None
TP12	40°C	20%	75%	1.0C	1.0C	None
TP13	40°C	20%	25%	1.0C	1.0C	None
TP14	40°C	80%	50%	0.5C	0.5C	None
TP15	40°C	80%	50%	0.2C	0.2C	None
TP16	40°C	80%	50%	1.0C	0.5C	None
TP17	40°C	80%	50%	0.5C	1.0C	None
TP18	40°C	80%	50%	1.0C	2.0C	None
TP19*	40°C	40%	50%	1.0C	2.0C	None

begin of life (BOL) in the respective cycle.

2.4. Testing procedure

Fig. 1 gives an overview of the testing procedure applied in this cycle aging study. For this aging study, 63 cells were selected from a pool of 1100 fresh cells from two batches (batch 1: 600 cells, batch 2: 500 cells) that had been previously examined with an initial reduced CU measurement [26]. A selection procedure was applied in order to select as homogeneous cells as possible for both the calendar and cycle aging study. After each CU, each cell was charged to the respective start SOC as defined by the test matrix (see Table 3) based on the actual capacity measured in the full discharge step of the prior CM.

Thereafter all cells were cycled with the conditions defined in the design of the experiments (see Subsection 2.5 and 2.6). In order to capture the changing aging behavior as a function of time, the cycle operation of the cells was interrupted in variable time intervals to do CU measurements. At the beginning of the study, the CU measurements were repeated every week for three periods, every 2 weeks for the next three periods and afterwards every 4 weeks. In the last quarter of the aging study, the CU measurements were carried out 2 times at 8 week intervals and continued with 6 week intervals until the end of the study. In total 35 CU of which 4 are extended CU measurements were performed during the aging study. The aging study was stopped (end of test (EOT)) after 970 days duration (885 days under cycle aging conditions) and completed with a final extended CU measurement.

Every TP was investigated with at least three cells. If not stated otherwise, the mean values are provided.

2.5. Static cycle aging

With the aim to accelerate the cyclic aging tests, higher temperatures were applied. In order to remain within the specifications of the cell, 45°C was chosen as the maximum ambient temperature for the cycle aging tests. For comparability with other aging studies, the slightly lower ambient temperature of 40°C was chosen as the main temperature for the cycle aging test points (TPs). For the verification of the measurements, some test points (TPs) are also defined at the reference temperature of 25°C .

The cyclic aging was investigated by applying test points (TPs) with constant C-rates and SOC-ranges. Based on the aging effects of the individual test points (TPs), the aging model was parameterized. The

cyclic test points (TPs) could ideally be matched to the possible stress values in realistic stationary battery energy storage system (BESS) applications. The evaluation of the dynamic load profiles (see Section 2.6) revealed, that cycles with DOCs < 5% dominate and the average C-rate is about 0.2C. Only in some cases, deeper cycles with higher C-rates occur. However, the investigated cell can be charged up to 1C and discharged up to 6C.

The minimum C-rate in the charge and discharge direction was set to be 0.2C because this is the average C-rate of the dynamic load profiles. Furthermore, it is to be expected that at low C-rates it is likely that cycle aging effects will not be noticeable because the calendar aging effects could dominate. As a reference test point, the load of 1C/1C (charge/discharge) was defined for different temperatures in order to evaluate the influence of the temperature on cycle aging independently of the calendar aging. Due to the fact that the C-rates vary in the course of real load profiles as well as in the dynamic load profiles used in this study, different combinations of charge and discharge rates were also tested with respect to this reference test point. Because only C-rates up to 1C can be expected in stationary BESS applications, the maximum discharge current was limited to 2C in order to accelerate the cycle aging.

In contrast to the battery application in electric vehicle (EV), there are no established test profiles for stationary applications. Depending on the application, the battery is charged and discharged with variable currents. Furthermore, the resulting cycle depths depend strongly on the application, on the dimensioning of the battery and the inverter. Hence, the test points (TPs) must cover different DOCs. In the dynamic load profiles, the average SOC is about 50%, which is typical for stationary applications. Thus, the test points (TPs) with DOCs smaller than 100% use medium SOC of 50%. However, two test points (TPs) with a higher and a lower medium SOC were applied to check the dependence of the aging effects on the average SOC.

Details on the static cycle aging test points (TPs) are provided in the following and summarized in Table 3. The average SOC column indicates the average SOC of the respective cycles with individual DOCs. For the test points (TPs) with the DOCs smaller than 100%, the DOC is related to the nominal capacity and the Ah-throughput per cycle is kept constant as long as the remaining, actual capacity allows. As soon as the voltage limits are reached as a result of the capacity loss, the Ah-throughput per cycle will drop continuously. The cycling of all test points (TPs) begins at the defined minimum SOC_{min} , which is obtained by subtracting half of the respective DOC from the average \overline{SOC} :

$$SOC_{min} = \overline{SOC} - \frac{DOC}{2} \quad (1)$$

After every CU, the average SOC is adapted with respect to the remaining capacity (CC and CV phase) determined in the preceding CM.

TP1-2: These test points (TPs) with a temperature of 25°C allow to verify whether the elevated temperature of 40°C in the reference TP 6 has an influence only on the calendar aging or also on the cycle aging.

TP3: This TP with a temperature of 25°C was added to analyze the influence of the DOC of 20% at a lower temperature than for the TP8.

TP4: This TP enables to analyze the influence of the CV phase in charge direction in comparison to the reference TP 6. The CV phase is stopped at a current of 100 mA, which is the datasheet value.

TP5: Compared to the TP4, in this TP the cycles are performed without a CV phase in order to be able to distinguish the aging effects of the CV phase. As opposed to the reference test point 6, the full SOC range is used. However, a DOC of 100% with respect to the nominal capacity is only possible at the beginning of the aging study. Similar to the TP4, the Ah-throughput per cycle will decrease continuously due to the expected cycle aging leading to less usable capacity.

TP6: This TP serves as the reference for the other test points (TPs).

TP7-11: In comparison with the reference TP6, the influence of the DOC can be investigated with these test points (TPs). The DOCs of 40%, 20%, 10%, 5% and 1% are examined. The smaller step size in the range

of smaller DOC is necessary because a stronger sensitivity of the cycle lifetime is expected here. The TP with 20% DOC is required as a reference to TP12 and TP13.

TP12-13: These test points (TPs) are cycled with the same DOC of 20% but around different average SOC than in TP8. 25% and 75% are chosen as average SOC because these SOC are also investigated in the static calendar aging study. Furthermore, this means that a constant Ah-throughput can still be achieved up to a capacity loss of 10%.

TP14-15: In comparison to the reference TP6, this TP is cycled with low C-rates in order to investigate the influence of lower currents on the cycle lifetime. It can be expected that the sensitivity of the C-rate is relatively high. Hence, in addition to the minimum C-rate of 0.2C, 0.5C is used to test the influence of the C-rate.

TP16-17: These test points (TPs) are used to examine the influence of unsymmetrical charge and discharge C-rates compared to the reference TP6. The charge and discharge rate is reduced to 0.5C in each case to meet with the reference of TP14 while enabling sufficient cycle throughput.

TP18-19: These test points (TPs) are used to evaluate the effects of larger discharge rates compared to reference TP6.

2.6. Dynamic cycle aging

In addition to static test points (TPs) with constant C-rates and DOC, a dynamic cycle aging study was performed with dynamic stress profiles. The results of these dynamic stress profiles were later used to validate the combined aging model (see Section 3.3.2).

In the *ESPEN* project [28], the two applications and the combined use of the PV-home energy storage system (PV-HESS) with the simultaneous provision of primary control reserve (PCR)-power (PV-PCR-BESS) have been investigated. For these two applications, measurements of the resulting currents for the battery were carried out in field tests by the *Fraunhofer Institute for Solar Energy Systems* (Fraunhofer ISE). Based on this measurement data, synthetic current profiles with a duration of less than 24 h were created, which represent the condensed profile characteristics over the course of one year. These so-called load collectives of the two applications have been used by Fraunhofer ISE et al. in aging studies in the *ESPEN* project and were also applied here for comparison.

These two load collectives/dynamic stress profiles were tested in the dynamic cycle aging study at an ambient temperature of 40°C with the same testing procedure as applied in the static calendar and cycle aging study (see Section 2.4). Due to capacity degradation in the course of the aging study, these profiles have to be adapted by updating the start SOC with respect to the remaining capacity as determined in the previous CM.

In the following, these two load collectives/dynamic stress profiles are briefly described. The main characteristics of both profiles are summarized in Table 4.

Table 4
Characteristics of the PV-HESS and PV-PCR-BESS profiles.

Characteristic/Profile	PV-HESS	PV-PCR
Duration	15.50 h	22.85 h
Resolution	1min	1min
Charge Ah-throughput	1.562 C_N	0.732 C_N
Discharge Ah-throughput	1.562 C_N	0.732 C_N
Average charge C-rate	0.243C	0.073C
Average discharge C-rate	0.172C	0.057C
Maximum charge C-rate	0.750C	0.359C
Maximum discharge C-rate	0.750C	0.285C
Average SOC	51.4%	51.2%
Minimum SOC	5.4%	36.3%
Maximum SOC	80.0%	61.4%

2.6.1. PV-HESS profile

This profile was created based on measurements of the consumption and photovoltaic (PV) feed-in data of a model house in the city of Freiburg with a PV-system but without a battery storage for a period longer than one year. These profiles were separated into a summer and a winter part and converted into load collectives. Currents in and out of the battery were defined as follows: If the PV power is greater than the household consumption and SOC less than 100%, the battery should be charged. If the PV power is less than the power requirement and the SOC is greater than 0%, the battery should be discharged. An efficiency of 100% was assumed. In order to generate a condensed test profile, frequencies of the measured profile were analyzed and synthetic data was generated in the form of a summer and winter day load collective. These two-day profiles were combined into a single profile, normalized to the nominal capacity of the Sony cell and shifted to a SOC range between 9% and 80%. A few load peaks over 0.75C were removed.

The following Fig. 2a shows the PV-HESS load collective with the C-rate and the resulting SOC-curve. Table 4.

2.6.2. PV-PCR-BESS profile

The PV-PCR-BESS profile is a synthetic load collective of a PV-HESS profile with a superimposed PCR-supply profile. The assumed BESS has an energy capacity of 10 kWh, the PV-system has a peak power of 10 kW of which 7.5 kW are available for PCR. The efficiency of the BESS was assumed to be 100%. The power line frequency of the European UCTE (Union for the Coordination of Transmission of Electricity) grid of the year 2012 was used to generate the PCR profile. The energy capacity of the BESS can only be used freely in the SOC range of 50%–60% due to the regulations of the PCR-market. Outside of these limits, only corrections are allowed to reach the setpoint SOC of 50%. Currents < 30 mA (values related to the measured application; minimum value of the measuring device) and time periods without load were removed, resulting in a profile of less than 24 h duration. This PV-PCR-BESS profile is shown in Fig. 2b with the C-rate and the resulting SOC-curve in comparison to the PV-HESS.

3. Results & discussion

In this section the results of the cycle aging study are presented and discussed. We then outline the combined aging model for the calendar and cycle aging and discuss the results of the model validation based on the dynamic cycle aging study.

Although a variety of parameters are available from the CU measurements, only the relative discharge capacity C_{disch} and relative resistance $R_{\text{DC},10\text{s}}$ are evaluated here, because they are the most representative parameters and commonly used in aging models for lifetime simulations.

C_{disch} is determined as the mean of the discharge capacity (CC + CV-

phase) in the two full cycles of the periodic CU (see Eq. (2)). $R_{\text{DC},10\text{s}}$ is defined as the voltage difference measured between the beginning of relaxation after a constant current pulse $V(t = 0\text{s})$ and after 10s of relaxation $V(t = 10\text{s})$ divided by the current of each pulse. Here, $R_{\text{DC},10\text{s}}$ is calculated as the mean value of $R_{\text{DC},10\text{s}}$ determined after a 1C discharge pulse (disch) and 1C charge pulse (ch) in the 4th phase of the CM during the periodic CU (see Eq. (3)).

$$C_{\text{disch}} = \frac{1}{2} (C_{\text{CC},1,\text{disch}} + C_{\text{CV},1,\text{disch}} + C_{\text{CC},2,\text{disch}} + C_{\text{CV},2,\text{disch}}) \quad (2)$$

$$R_{\text{DC},10\text{s}} = \frac{1}{2} \left(\frac{V_{0\text{s}} - V_{10\text{s}}}{I_{\text{disch}}} + \frac{V_{0\text{s}} - V_{10\text{s}}}{I_{\text{ch}}} \right) \quad (3)$$

3.1. Aging results

3.1.1. Capacity and resistance measurements

Here the results of the cycle aging test points (TPs) are shown separated into the single influence parameters on cycle aging, C-rate, DOC around a fixed SOC, and fixed DOC around different SOC. The data shown in the following figures represents the total aging and includes, therefore, calendar aging. For the creation of the aging models in Section 3.2, the calendar aging results are subtracted from the total aging results shown here. For the same reason, the temperature influence is investigated in Section 3.1.4, because the calendar aging influence has to be taken into account.

3.1.2. Influence of C-rate

Fig. 3 shows the development of the relative discharge capacity C_{disch} and the relative resistance $R_{\text{DC},10\text{s}}$ for selected cycle aging test points (TPs) with different C-rates but all with $\text{DOC} = 80\%$ cycles around $\text{SOC} = 50\%$ at 40°C . The degradation over the whole aging study with 35 CU measurements is shown in the upper panel as a function of time and in the lower panel as a function of Ah-throughput.

The relative discharge capacity is decreasing for all C-rates over time, see Fig. 3a, and over FEC, see Fig. 3c, and follows approximately a square root linear relation of time as well as of FEC. This is in agreement with [11,22].

The cell resistance increases for all C-rates over time, see Fig. 3b, and over FEC, see Fig. 3d, but in contrast to the capacity fade, the rate of increase remains constant over time as well as over FEC.

The loss of C_{disch} over time in Fig. 3a and the increase of $R_{\text{DC},10\text{s}}$ in Fig. 3b, are both more severe for higher charge and discharge C-rates. However, the relative capacity decrease is almost double the relative resistance increase for the respective test points (TPs). When assuming that SEI growth is the dominating aging effect for calendar and cycle aging, the Ah-throughput would be the most important influence factor in cycle aging. Plotting the degradation over FEC instead of time of C_{disch} in Fig. 3c and $R_{\text{DC},10\text{s}}$ in Fig. 3d suggests that higher charge and discharge

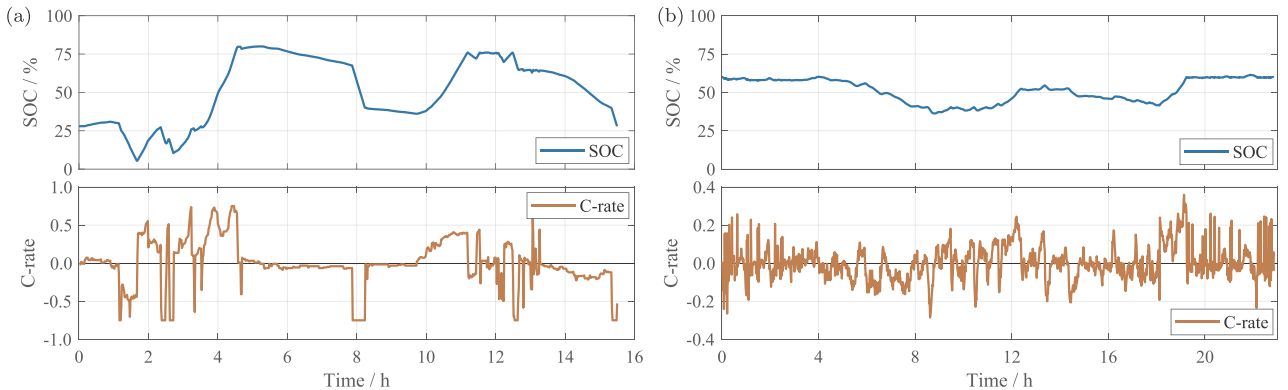


Fig. 2. a) PV-home energy storage system (PV-HESS) profile and b) PV-PCR-BESS profile: The upper plots show the SOC profile, the lower plots show the C-rate profile.

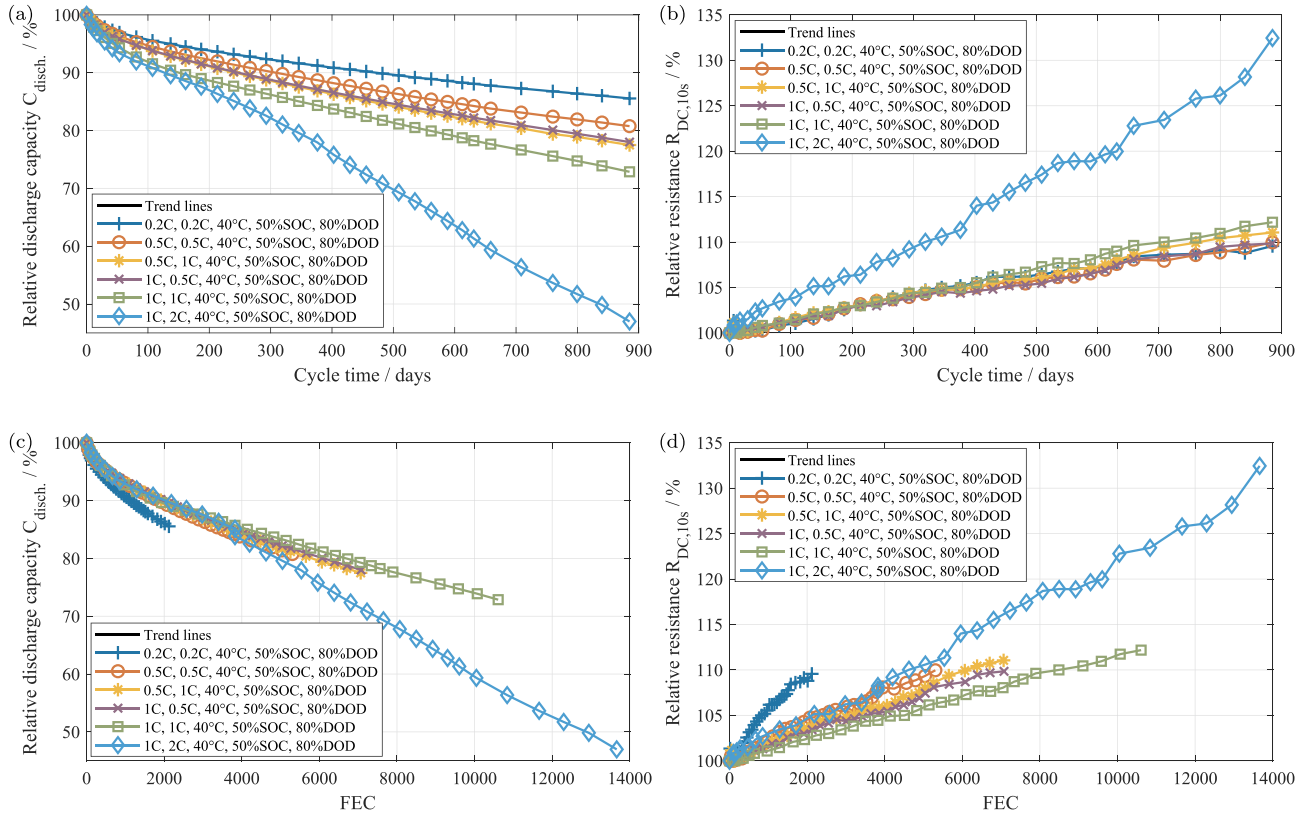


Fig. 3. Degradation over 885 days of selected cycle aging test points (TPs) with different C-rates with $DOC = 80\%$ around $SOC = 50\%$ at $40^\circ C$: (a) Relative discharge capacity C_{disch} over time. (b) Relative resistance $R_{DC,10s}$ over time. (c) Relative discharge capacity C_{disch} over FEC. (d) Relative resistance $R_{DC,10s}$ over FEC. All values are related to the measurements of the first CM. Each subplot shows the mean values of the three cells of each TP. Legend entries: Charge current, discharge current, temperature, mean SOC, DOC.

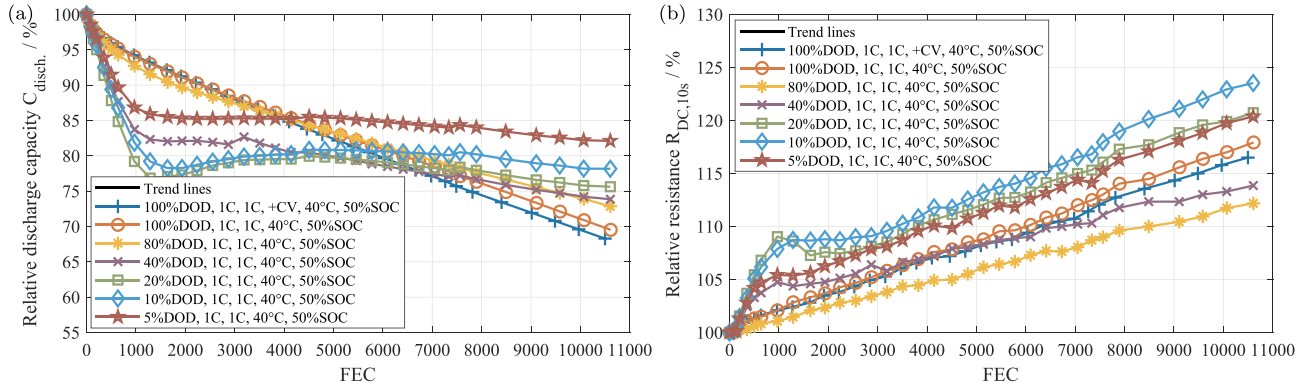


Fig. 4. Degradation over 885 days of selected cycle aging test points (TPs) with different DOC around $SOC = 50\%$ all with 1C in charge and discharge direction at $40^\circ C$ over FEC. DOC : (a) Relative discharge capacity C_{disch} . (b) Relative resistance $R_{DC,10s}$.

C-rates lead to smaller rates of decrease or increase of the two parameters, respectively. However, when the calendar aging is subtracted, it becomes clear that higher C-rates lead to stronger aging than lower C-rates (see Section 3.2.4). Only for the TP with 2C discharge, a change of the degradation rate occurs after about 4000 FEC, which might be induced by an additional aging mechanism like lithium plating [8].

3.1.3. Influence of DOC

Fig. 4 shows the evolution of the relative discharge capacity C_{disch} and the relative resistance $R_{DC,10s}$ for selected cycle aging test points (TPs) with different DOC around $SOC = 50\%$. All feature a 1C rate in charge and discharge direction at $40^\circ C$ over FEC. The degradation trends

vary considerably as a function of DOC. Only for the higher $DOCs = 80\%$ and 100% , degradation follows a approximately a square root linear dependence on time/FEC for C_{disch} and a linear trend for $R_{DC,10s}$. Surprisingly, for lower $DOCs$, we can observe an almost linear degradation of C_{disch} in Fig. 4a and of $R_{DC,10s}$ in Fig. 4b until about 1000 FEC. The highest degradation rates occurred for $DOCs = 10\%$ and 20% . Since the $DOCs = 5\%$ and 40% produced lower degradation rates, no clear correlation between DOC and the rate of degradation can be established. From 1000 FEC onwards the rate of capacity fade for the test points (TPs) with $DOCs < 80\%$ levels off for at least 2000 FEC before it again slightly increases. For the $DOCs = 10\%$ and 20% , which produced the strongest capacity decrease in the beginning, the capacity even increases

between 1000 FEC and 5000 FEC. Finally, at the EOT at about 10600 FEC the total capacity losses are higher for higher DOC. The resistance increase after the first 1000 FEC is almost linear for all test points (TPs). At EOT, no clear correlation between DOC and the absolute resistance increase can be observed.

A detailed investigation into the accelerated, partly reversible capacity loss with $DOCs < 80\%$ is ongoing.

3.1.4. Influence of temperature

The temperature influence on the pure cycle aging are evaluated based on the cycle aging test points (TPs) at 25°C and 40°C after subtracting the calendar aging. Calendar aging is evaluated based on the calendar aging model presented in the previous study [1]. The DOCs were 80% and 100% around $SOC = 50\%$ at 1.0C. The results are shown in Fig. 5a for $Q_{loss,cyc}$ and in Fig. 5b for $R_{inc,cyc}$. For the test points (TPs) with $DOC = 80\%$ at 25°C and 40°C ambient temperatures, the trend lines of both $Q_{loss,cyc}$ and $R_{inc,cyc}$ are in a good accordance from the beginning until about 8000 FEC, despite the temperature difference. For the test points (TPs) with $DOC = 100\%$ at 25°C and 40°C ambient temperatures, the trend lines of both $Q_{loss,cyc}$ and $R_{inc,cyc}$ first follow the same course but start to differ after 4000 FEC.

Although the temperatures 25°C and 40°C do not cover the entire operating temperature range of the cells, this temperature range can be assumed to be the target temperature for the BESS operation since lower and higher temperatures lead to accelerated degradation of both capacity and resistance.

3.2. Cycle aging model development

3.2.1. Model limitations

The aging model that is outlined in the following section is empirical and incorporates only those influence factors and parameters that have been investigated experimentally. For example, as the temperature influence on pure cycle aging between 25°C and 40°C was found to be negligible, the model does not consider a temperature influence on cycle aging. As mentioned in Section 1.2, with temperatures lower than 25°C or higher than 40°C, additional aging effects can be expected. Furthermore, in contrast to the static calendar aging study, the measurement data of the static cycle aging showed no capacity increase or resistance decrease at the beginning of the aging study. While capacity effects related to the anode overhang area can be expected for the cycle aging test points (TPs) as well, they are not covered by the aging model. Finally, the test points (TPs) with $DOCs < 80\%$ exhibited unsteady aging trends with periods in which lost capacity was recovered. This is a phenomenon which needs to be investigated more thoroughly before it can be incorporated into the aging model.

3.2.2. Model structure

With the aim to create a combined aging model by superimposing a calendar aging and a cycle aging model, the cycle aging model has to represent the pure cycle aging. Therefore, the respective calendar aging of each TP is subtracted from the cycle aging results. Furthermore, the cycle aging model should reflect the individual influences on aging of the C-rate, the DOC, and the Ah-throughput in FEC. Similar to the calendar aging model, the cycle aging model should be described by expressions that only contain the relevant influence parameters (C-rate, DOC, and FEC) and a small set of constants that are determined separately for each influence parameter.

Consequently, Q_{loss} and R_{inc} are expressed by a product of three factors that represent the influence of C-rate with $k_{C-rate, Q_{loss}/R_{inc}}$ (C-rate), of DOC with $k_{DOC, Q_{loss}/R_{inc}}$ (DOC) and of FEC individually. Please see Eq. (5). The factors are derived separately in the following and their parameters are shown in Table 6. The general combined and cycle aging equations are provided in Table 5.

3.2.3. Influence of Ah-throughput/FEC

For all cycle aging test points (TPs), the capacity loss follows approximately a square root dependence of the Ah-throughput/FEC for different C-rates and DOC (see Figs. 3c and 4a). The Ah-throughput is therefore represented by the exponential factor $z_{Q_{loss}}^{cyc} = 0.5$. In contrast, the resistance increases rather linearly over the Ah-throughput/FEC for all C-rates and DOC (see Figs. 3d and 4b). The Ah-throughput/FEC is therefore represented by the exponential factor $z_{R_{inc}}^{cyc} = 1$.

3.2.4. Influence of C-rate

For the parameterization of the C-rate influence factor $k_{C-rate, Q_{loss}/R_{inc}}$ (C-rate), only the cycle aging test points (TPs) which feature equal charge and discharge C-rates are evaluated. They differ only in the C-rate and thus the test points (TPs) with $DOC = 80\%$

Table 5

General aging equations: The equations structure is equal for Q_{loss} and R_{inc} . Hence, only the equations of the capacity loss are shown.

General combined aging: (4)

$$Q_{loss}^{comb. [\%]} = Q_{loss}^{cal.} + Q_{loss}^{cyc.}$$

General cycle aging: (5)

$$Q_{loss}^{cyc.} = k_{T, Q_{loss}}^{cyc.} \cdot k_{C-rate, Q_{loss}}^{cyc.} \cdot k_{DOC/SOC, Q_{loss}}^{cyc.} \cdot FEC^{z_{Q_{loss}}^{cyc.}}$$

Cycle aging FEC variant: (6)

$$\frac{dQ_{loss}^{cyc.}}{dFEC} = z_{Q_{loss}}^{cyc.} \cdot k_{T, Q_{loss}}^{cyc.} \cdot k_{C-rate, Q_{loss}}^{cyc.} \cdot k_{DOC/SOC, Q_{loss}}^{cyc.} \cdot (FEC^{z_{Q_{loss}}^{cyc.}} - 1)$$

Virtual Ah-throughput FEC^* to consider change of aging influence factors: (7)

$$FEC_{Q_{loss}}^{*cyc.} = \left(\frac{Q_{loss}^{comb. tot. (FEC)}}{k_{T, Q_{loss}}^{cyc.} \cdot k_{C-rate, Q_{loss}}^{cyc.} \cdot k_{DOC/SOC, Q_{loss}}^{cyc.}} \right)^{\frac{1}{z_{Q_{loss}}^{cyc.}}}$$

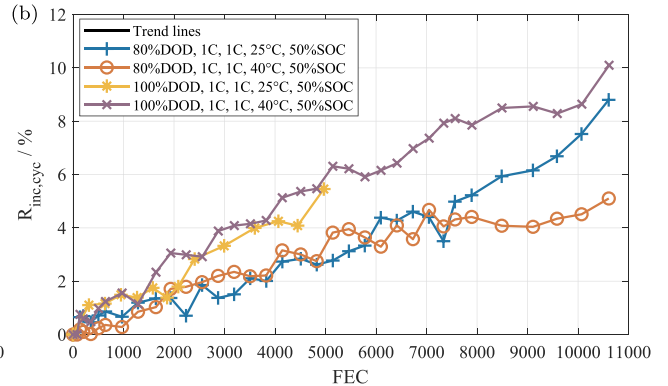
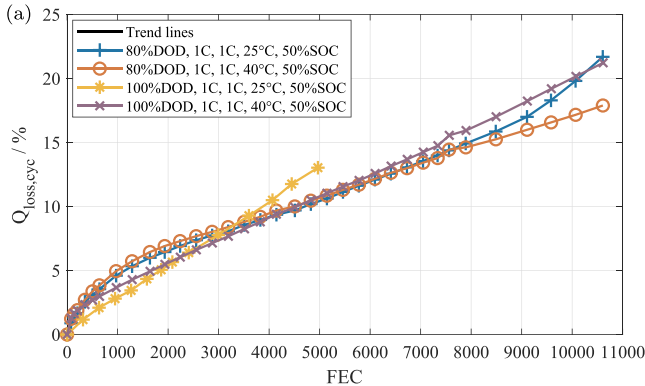


Fig. 5. Influence of the temperature on the pure cycle aging of $Q_{loss,cyc}$ and $R_{inc,cyc}$ for the test points (TPs) with $DOC = 80\%$ and 100% cycles around $SOC = 50\%$ for the C-rate 1.0C. (a) $Q_{loss,cyc}$. (b) $R_{inc,cyc}$.

Table 6 Q_{loss} and R_{inc} aging model reference values and parameters.

Parameter	Influence factor	Q_{loss}	R_{inc}
a	C-rate	0.0630	0.0020
b	C-rate	0.0971	-0.0021
c	DOC	4.0253	6.8477
d	DOC	1.0923	0.91882
$z_{Q_{loss}}^{cyc}$	FEC	0.5	1

around $SOC = 50\%$ at $40^\circ C$ are selected. To obtain the pure cycle aging values $Q_{loss,cyc}$ and $R_{inc,cyc}$ of these test points (TPs), the measured calendar aging $Q_{loss,cal}$ and $R_{inc,cal}$ of the TP with $SOC = 50\%$ at $40^\circ C$ are subtracted. The pure cycle aging results are shown in Fig. 6b for $Q_{loss,cyc}$ and in Fig. 6d for $R_{inc,cyc}$.

In order to model the sole influence of the C-rate with the factor $k_{C-rate, Q_{loss}/R_{inc}}$ (C-rate), the DOC influence factor $k_{DOC, Q_{loss}}(DOC)$ is set to the value of 1 for evaluation of the C-rate influence with the selected test points (TPs). The C-rate influence factor $k_{C-rate, Q_{loss}/R_{inc}}$ (C-rate) can be modeled for Q_{loss} and R_{inc} using the same formula with different parameter values a and b , see Eq. (8):

$$k_{C-rate, Q_{loss}/R_{inc}}(C-rate) = a_{Q_{loss}/R_{inc}} \cdot C-rate + b_{Q_{loss}/R_{inc}} \quad (8)$$

To obtain the parameters a and b , the C-rate influence factor $k_{C-rate, Q_{loss}/R_{inc}}$ (C-rate) is determined by fitting separately the aging curves of $Q_{loss,cyc}$ and $R_{inc,cyc}$ of the single C-rates with Eq. (5).

The resulting $k_{C-rate, Q_{loss}/R_{inc}}$ (C-rate) of the single C-rates are shown in Fig. 6a for $Q_{loss,cyc}$ and Fig. 6c for $R_{inc,cyc}$. Then, the parameters a and b are obtained by curve fitting using Eq. 8.

For $Q_{loss,cyc}$ the $k_{C-rate, Q_{loss}}$ (C-rate) values match a linear trend line

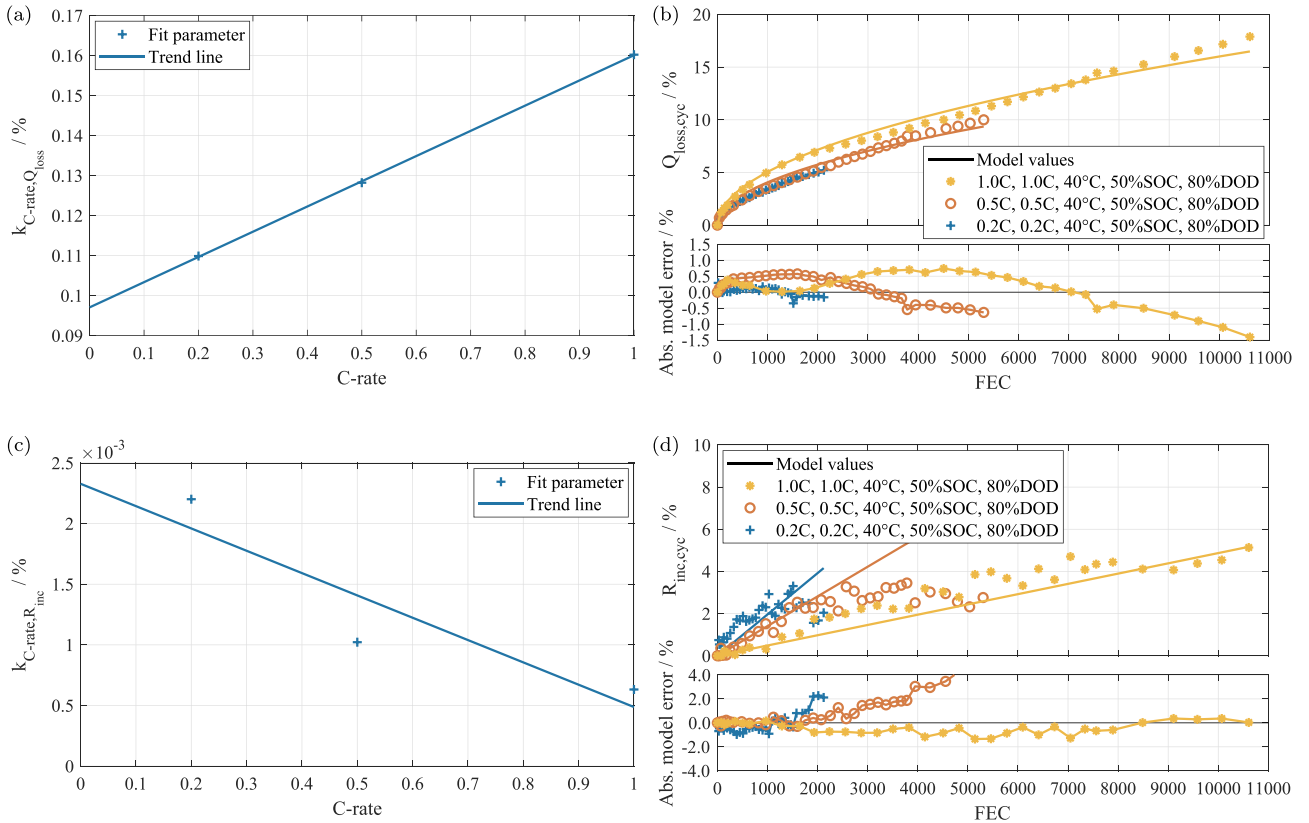


Fig. 6. Influence of the C-rate on the pure cycle aging of Q_{loss} and R_{inc} for the test points (TPs) with $DOC = 80\%$ cycles around $SOC = 50\%$ at $40^\circ C$ for the C-rates 0.2C, 0.5C and 1.0C: (a) $k_{C-rate, Q_{loss}}$ (C-rate) determined by fitting separately the aging curves of $Q_{loss,cyc}$ of the single C-rates with Eq. (5). (b)/(d) Comparison of measured values of Q_{loss}/R_{inc} with model values determined by Eq. (5) and using the $k_{C-rate, Q_{loss}/R_{inc}}$ (C-rate) values determined by Eq. (8). The lower panels show the absolute model error in %.

over the evaluated C-rates. The resulting aging model curves are compared in the upper panel of 6b with the measured values. The absolute model errors for the capacity loss $Q_{loss,cyc}$ is illustrated in the lower panel of Fig. 6b. For the TP with the C-rates 0.2C and 0.5C, the model error remains below $\pm 0.5\%$. For the TP with 1.0C, the model errors are still lower than $\pm 1.5\%$ at EOT. In contrast to the very clear trends of $Q_{loss,cyc}$, the pure cycle aging resistance increase values $R_{inc,cyc}$ fluctuate around a linear trend shown in Fig. 6d. The absolute model errors for $R_{inc,cyc}$ are shown in the lower panel of Fig. 6d: Only for the TP with 1C, the model captures the determined pure cycle aging $R_{inc,cyc}$ quite well, with errors below 2%. For the lower C-rates 0.2C and 0.5C, the model is accurate only in the first 3000 FEC. At higher FECs, strong deviations in $R_{inc,cyc}$ occur.

3.2.5. Influence of DOC

As shown in Fig. 4a and b, DOC and $Q_{loss,cyc}$ and $R_{inc,cyc}$ do not correlate. Again, the capacity loss and resistance increase due to the pure cycle aging are evaluated by subtracting the measured calendar aging $Q_{loss,cal}/R_{inc,cal}$ of the TP with $SOC = 50\%$ at $40^\circ C$. The results are shown in Fig. 7b for $Q_{loss,cyc}$ and in Fig. 7d for $R_{inc,cyc}$. Since the capacity loss of test points (TPs) with $DOC < 80\%$ shows several trend changes whose underlying mechanisms are unknown at this point, the model is parametrized based on the aging trends of test points (TPs) with $DOC = 80\%$ and 100% . The validation efforts show that, in spite of this drawback, the model accuracy in real-life scenarios is sufficient. The formula for $k_{DOC, Q_{loss}}(DOC)$ is derived by evaluating Eq. (9) with $Q_{loss,cyc}$ at EOT. The values of $k_{DOC, Q_{loss}}(EOT)(DOC)$ at EOT are shown in Fig. 7a over the respective DOC. The trend line matches the DOC influence on $k_{DOC, Q_{loss}}(DOC)$ and can be obtained by using Eq. (10) and deriving the parameters c and d (see Table 6) by curve fitting.

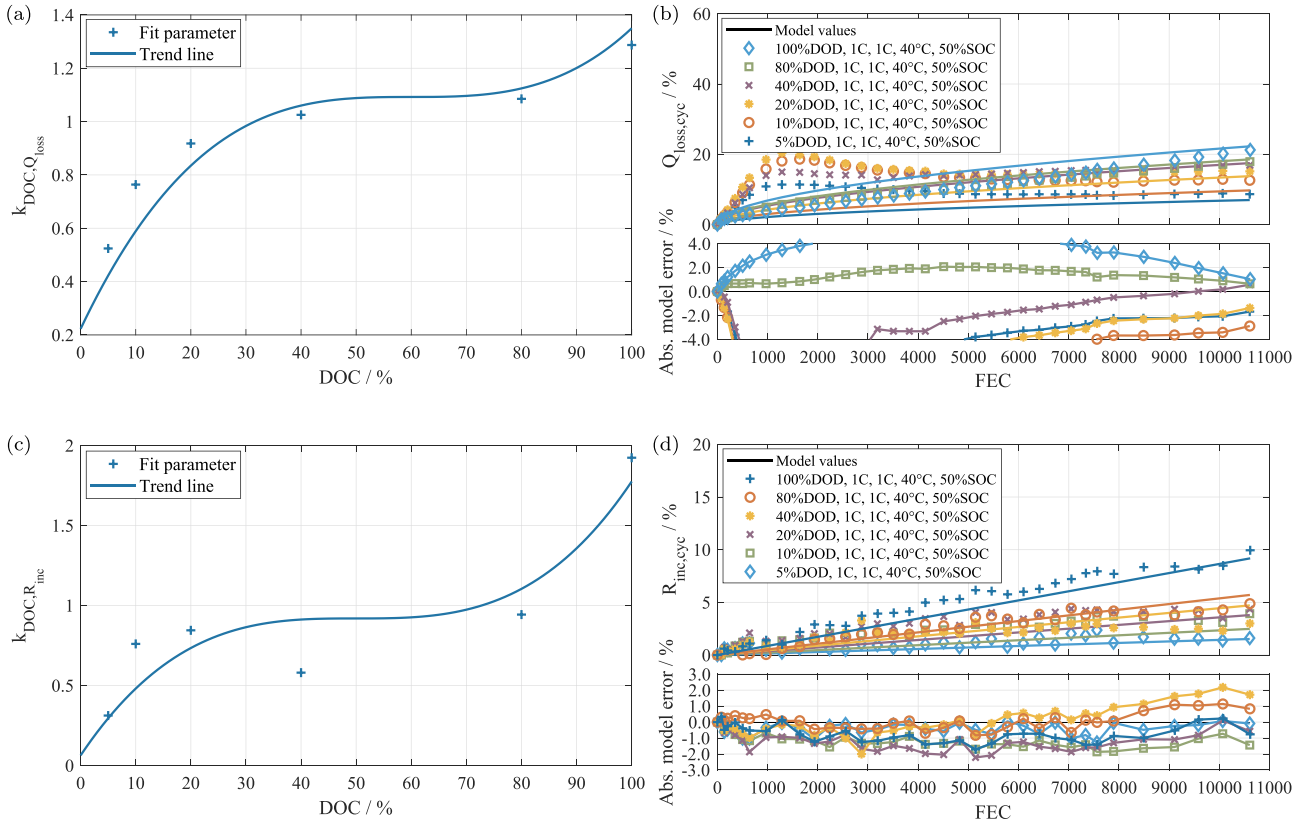


Fig. 7. Influence of the DOC on the pure cycle aging of $Q_{loss,cyc}$ and $R_{inc,cyc}$ for the test points (TPs) with 1.0C cycles around SOC = 50% at 40°C with DOC = 5%, 10%, 20%, 40%, 80% and 100%: (a) $k_{DOC,Q_{loss}}(DOC)$ determined by fitting separately the aging values at EOT of $Q_{loss,cyc}$ of the single DOC with Eq. (5). (b) Comparison of measured values of $Q_{loss,cyc}$ with model values determined by Eq. (5) and using the $k_{DOC,Q_{loss}}(DOC)$ values determined by Eq. (6). The lower panels show the absolute model error in %. (c) $k_{DOC,R_{inc}}(DOC)$ determined by fitting separately the aging values at EOT of $R_{inc,cyc}$ of the single DOC. (d) Comparison of measured values of $R_{inc,cyc}$ and using the $k_{DOC,R_{inc}}(DOC)$ values. The lower panels show the absolute model error in %.

$$k_{DOC,Q_{loss}}(DOC) = \frac{Q_{loss,cyc}(C - rate = 1C, DOC, FEC)}{k_{C-rate,Q_{loss}}(C - rate = 1C) \cdot \sqrt{FEC_{end}}} \quad (9)$$

$$k_{DOC,Q_{loss}}(DOC) = c_{Q_{loss}}(DOC - 0.6)^3 + d_{Q_{loss}} \quad (10)$$

In the upper panel of Fig. 7b, the results of Eq. (5) with the model values of $k_{DOC,Q_{loss}}(DOC)$ are compared to the pure cycle aging capacity loss. The absolute model errors shown in the lower panel are large at first but decrease near EOT since the model was fitted to the values at EOT. The DOC influence on the resistance increase of pure cycle aging is modeled similarly to the capacity loss. The formula for $k_{DOC,R_{inc}}(DOC)$ is derived by evaluating Eq. (11) with the $R_{inc,cyc}$ at EOT.

$$k_{DOC,R_{inc}}(DOC) = \frac{R_{inc,cyc}(C - rate = 1C, DOC, FEC)}{k_{C-rate,R_{inc}}(C - rate = 1C) \cdot FEC_{end}} \quad (11)$$

$$k_{DOC,R_{inc}}(DOC) = c_{R_{inc}}(DOC - 0.5)^3 + d_{R_{inc}} \quad (12)$$

The values of $k_{DOC,R_{inc}}(EOT)(DOC)$ at EOT are shown in Fig. 7b over the respective DOC. The trend line represents the DOC influence on $k_{DOC,R_{inc}}(DOC)$ for most of the DOC, however, the deviations are bigger than for $k_{DOC,Q_{loss}}(DOC)$, see Fig. 7a. Again, Eq. (12) is applied and the parameters c and d (see Table 6) are derived by curve fitting. The results of Eq. (5) using the model values of $k_{DOC,R_{inc}}(DOC)$ are compared to the determined resistance increase of pure cycle aging in the upper panel of Fig. 7d. The model trend lines follow the pure cycle aging resistance for all DOC, however, due to the fluctuating values of the resistance increase, the model error alternates between $\pm 2.0\%$ for all DOCs.

3.2.6. Validation

To apply the cycle aging model equations with varying C-rates or

DOCs over FEC to a lifetime simulation, a differential form of the cycle aging models is derived. Eq. (5) is differentiated with respect to FEC for $Q_{loss,cyc}$, which yields Eq. (6). The same procedure is applied to $R_{inc,cyc}$. Similar to the calendar aging model presented in Ref. [1], it is necessary to determine how to apply the cycle aging models correctly when the cycle influence factors vary. The dynamic calendar aging study proved the independence of the order of storage conditions and that the calendar aging rate is dependent on the current (SOH). The same approach is applied for the pure cycle aging model, however, to determine the differential capacity loss $q_{loss,cyc}$ when varying the cycle influence factors, a virtual Ah-throughput with FEC^* is defined, representing the FEC until the same $Q_{loss,cyc}$ is reached under the new cycle conditions. As the resistance increase due to pure cycle aging is constant over FEC, no additional measures for Ah-throughput compensation of R_{inc} have to be taken. The virtual FEC^* can be derived by solving Eq. 5 for FEC. This results in Eq. (7) for $Q_{loss,cyc}$. When using the cycle aging model with variable cycle influence factors, the virtual FEC^* has to be determined for each step. Then FEC^* is used to calculate the differential capacity loss $\frac{dQ_{loss,cyc}}{dFEC}$ (see Eq. (6)) in the next interval with new cycle conditions.

The pure cycle aging models cannot be validated on its own because aging during dynamic stress profiles is always a superposition of calendar and cycle aging. One option would be a dynamic validation profile with low temperature, where only a minor influence of calendar aging can be expected. However, at low temperatures, additional cycle aging due to lithium plating could occur which are not represented by this cycle aging model.

Another way to validate the cycle aging model would be the comparison with the datasheet values for the investigated cell. However, the datasheet provides aging data only for full cycles with a DOC = 100% and a

C-rate of 1.0C at 23°C, for which it states a relatively broad range of 6000 to 10.000 FEC before reaching 20% capacity loss. Furthermore, data-sheet values usually include the calendar aging effect. As neither option for individual validation of the cycling aging model seems promising, the cycle aging model is validated in conjunction with the calendar aging model using dynamic stress profiles.

3.3. Combined aging model

3.3.1. Model structure

In order to estimate the calendar and cycle aging in lifetime simulations of BESS, a combined aging model is developed and presented here. Since the cycle aging model represents only the pure cycle aging without calendar aging, a combined aging equation for the capacity loss can be established as a simple superposition of the calendar aging model [1] with the cycle aging model Eq. (5), resulting in the combined aging model in Eq. (4).

3.3.2. Validation

The combined aging model is validated with the results of the dynamic cycle aging study. The two load profiles presented in Section 2.6 are used at an ambient temperature of 40°C. During cycling of the cells, their temperature rose from 40°C to a mean value of 40.8°C for the PV-HESS profile and 40.6°C for the PV-PCR-BESS profile. These temperatures are used to estimate the combined aging since temperature has a significant impact on calendar aging. Within the 885 days of the aging study, the PV-HESS profile was completed 1368 times and the PV-PCR-BESS profile 928 times. To calculate the combined aging, the load profile

stress is characterized by the half-cycle detection algorithm (included in the BESS model framework software for techno-economic simulation of stationary energy storage systems (SimSES) [29]) applied to the original SOC-course of both profiles. It determines DOC, mean C-rate and mean SOC of every half-cycle. After every half-cycle, the calendar and cycle aging is calculated and summed up to obtain the combined aging.

Fig. 8 shows the development of the capacity loss $Q_{loss,meas}$ and resistance increase $R_{inc,meas}$ for the PV-HESS profile on the left side and for the PV-PCR-BESS profile on the right side. In addition to the combined aging for $Q_{loss,comb.}$ and $R_{inc,comb.}$, the individual calendar and pure cycle aging contributions are shown for both profiles.

3.3.2.1. PV-HESS profile. For the PV-HESS profile, the aging model results follow the measured capacity loss closely and deviate only about 0.5% at EOT. The estimated capacity loss due to calendar aging at EOT, $Q_{loss,cal} = 9.21\%$, matches well the capacity loss of $Q_{loss,cal} = 9.24\%$, measured in the static calendar static aging in TP at 40°C with SOC = 50%. The capacity loss due to pure cycle aging is $Q_{loss,cyc} = 3.64\%$. It represents 28.35% of the estimated combined aging.

For the resistance, the combined aging model results follow the measured trend closely in the first 500 days, then, however, the model error grows up to 2%. This deviation originates mainly in the model error of cycle aging, since the resistance increase due to calendar aging at EOT with $R_{inc,cal} = 8.07\%$ exceeds only slightly the resistance increase measured within the static calendar static aging study with $Q_{loss,cal} = 7.31\%$ (TP at 40°C with a SOC = 50%). The resistance increase due to pure cycle aging is $R_{inc,cyc} = 2.80\%$ and represents

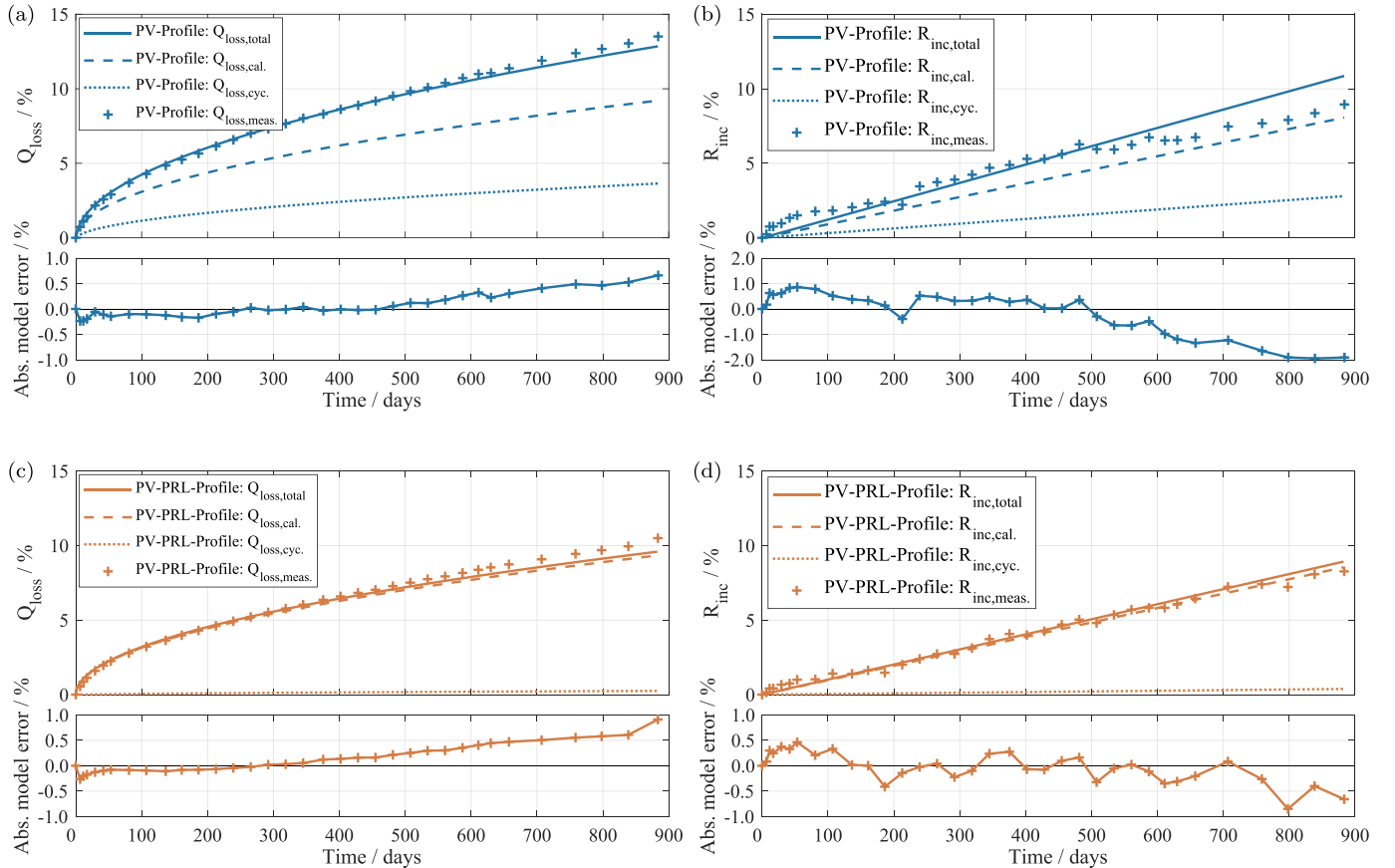


Fig. 8. Combined aging model validation with the aging results of the dynamic cycle aging study with the two load profiles operated over 885 days at 40%. Each plot shows the mean values of the measured $Q_{loss,comb.}/R_{inc,comb.}$ of the three cells of each load profile. The plots on the left side represent the capacity loss and the plots on the right side resistance increase of the respective load profile. Additional to the estimated combined aging, the particular fractions of the calendar and pure cycle aging are drawn in every plot. The lower panel in every plot shows the absolute model error in % compared to the measured values. (a/b) PV-HESS load profile (c/d) PV-PCR-BESS load profile.

25.74% of the estimated combined aging.

3.3.2.2. PV-PCR-BESS profile. For the PV-PCR-BESS profile, the aging model captures the capacity loss well and deviates about 1% at EOT. The estimated capacity loss due to calendar aging at EOT, $Q_{\text{loss,cal}} = 9.34\%$, matches well the capacity loss $Q_{\text{loss,cal}} = 9.24\%$, measured in the static calendar static aging with the TP at 40°C with a $\text{SOC} = 50\%$

The capacity loss due to pure cycle aging is $Q_{\text{loss,cyc}} = 0.25\%$ and represents 2.61% of the combined estimated aging. This small contribution of cycle aging can be explained by the characteristics of the PV-PCR-BESS profile, which contains mainly small half-cycles with $\text{DOC} < 1\%$.

The model errors for the resistance are small, too, at $< 1\%$. Similar to the capacity loss, the resistance increase due to pure cycle aging represents only 4.28% of the combined estimated aging resulting in $R_{\text{inc,cyc}} = 0.38\%$.

A possible systematic source of error could be the neglect of the capacity decrease in the half-cycle characterization: The load profiles' DOC, mean C-rates and SOC values were determined only for the raw load profiles at BOL. During the aging study, the capacity decrease leads to larger DOC, C-rates and SOC values since the current profile is independent of the SOH. In contrast, when using the BESS simulation framework SimSES this adaption is made after every single half-cycle leading to more accurate results of the estimated cycle aging [29].

In conclusion, the results of the combined aging model validation with these two dynamic load profiles demonstrate, that the pure cycle aging model is able to estimate the capacity loss and the resistance increase with sufficient precision even on a long time scale with dynamic profiles.

4. Conclusions

We performed a cycle aging study of a LFP/C cell including more than 19 test points (TPs) with 3 cells per TP and a duration of almost 900 days. Based on the results and a previous calendar aging study and model, a combined cycle/calendar aging model was developed. The model was validated against experimental measurements using synthetic load profiles for stationary storage application.

The results of the cycle aging study reveal a strong influence of the DOC and SOC on both capacity loss and resistance increase. The capacity degradation of the test points (TPs) with $\text{DOCs} = 80\%$ and 100% follows a square root dependence of time/FEC for C_{disch} and a linear trend for $R_{\text{DC},10s}$. For the test points (TPs) with lower DOC, however, the capacity degradation rates are higher at first and follow linear trends, but level off after about 1000 FEC. At EOT at about 10600 FEC, the final capacity losses are higher for bigger DOC, showing the expected influence of DOC on the capacity loss. In contrast to the capacity degradation trends, the resistances increased for all test points (TPs) with an almost linear trend. For both capacity and resistance degradation, cycling with $\text{DOCs} = 20\%$ around $\text{SOC} = 50\%$ lead to higher aging than lower and higher SOC-ranges.

The C-rate showed only small influence on capacity loss and resistance increase, however, higher degradation rates were observed for the relatively high discharge C-rate of 2C at 40°C.

Since the measured aging values were adjusted for calendar aging, which contains most of the temperature-related aging effect, the pure cycle aging results showed almost no influence of temperature for the investigated temperature range of 25°C to 40°C.

Based on the static cycle aging study, a semi-empirical model was developed to estimate Q_{loss} and R_{inc} for the influence of C-rate, DOC, and Ah-throughput. The resulting aging equations are products three factors, each representing one of the influence parameters. The Ah-throughput is considered with a square root of the FEC for the capacity loss and with a linear influence on the resistance increase. The influence of the C-rate on the degradation is modeled with a linear factor with higher values at

higher C-rates for the capacity loss. For the resistance increase, the C-rate influence factor is modeled with an inverse trend over the C-rate with respect to the measured results. Due to the incoherent aging trends for different DOC, only the values at EOT and the trends of the test points (TPs) with $\text{DOCs} = 80\%$ and 100% were used for the model development. Finally, a cubic trend over the DOC was used to model the influence of the DOC with good accordance for the values at EOT.

The combined aging model was validated with two dynamic load profiles PV-HESS and PV-PCR-BESS over a period of almost 900 days. The simulated capacity losses and resistance increases matches the measurement results well. The absolute model errors were consistently below 1% for the capacity loss and 2% for the resistance increase. Consequently, the developed aging model is considered to be sufficiently accurate for lifetime estimates of BESS applications.

5. Outlook

The developed aging model of the investigated LFP/C cell successfully captures the cell aging in dynamic load profiles, but the general limits of the semi-empirical aging modeling approach still apply: Without realistic cause-effect relationships, like in physico-chemical models, the model cannot make trustworthy predictions about cycle aging at much lower or higher temperatures or C-rates than those applied in the measurements that were used for parametrization. In consequence, further studies need to expand the range of parameter values of the influencing factors and/or analyze individual aging effects with a physico-chemical approach.

Also not considered in the model was the significant, partly-reversible capacity loss with shallow cycles that occurred in the cycle study. Its consequences in application may be limited: In the realistic, dynamic load profiles with dynamic SOC-ranges, the effect did not occur. However, it is a highly interesting phenomenon that will be the subject of a follow-up publication.

Declaration of competing interest

The authors declare that they have no known competing financial interests or personal relationships that could have appeared to influence the work reported in this paper.

Acknowledgements

This work was financially supported by the Bavarian Ministry of Economy, Media, Energy and Technology under the auspices of *EEBatt* and by *TUM (Technical University of Munich, Germany)* and *NTU (Nanyang Technological University, Singapore)* within the joint project agreement *ICER (International Center of Energy Research)*. The responsibility for this publication rests with the authors.

Appendix A. Supplementary data

Supplementary data to this article can be found online at <https://doi.org/10.1016/j.jpowsour.2019.227666>.

Acronyms

BESS	battery energy storage system
BOL	begin of life
CC	constant-current
CM	capacity measurement
CTS	cell test system
CU	check-up
CV	constant-voltage
DOC	depth of cycle
DVA	differential voltage analysis
EIS	electrochemical impedance spectroscopy

EOL	end of life
EOT	end of test
EV	electric vehicle
FEC	full equivalent cycle
LAM	loss of active material
LFP	lithium iron phosphate
LLI	loss of lithium inventory
OCV	open circuit voltage
PCR	primary control reserve
PV	photovoltaic
PV-HESS	PV-home energy storage system
SEI	solid electrolyte interphase
SimSES	software for techno-economic simulation of stationary energy storage systems
SOC	state of charge
SOH	state of health
TP	test point

References

- [1] M. Naumann, M. Schimpe, P. Keil, H.C. Hesse, A. Jossen, Analysis and modeling of calendar aging of a commercial lifepo4/graphite cell, *Journal of Energy Storage* 17 (2018) 153–169, <https://doi.org/10.1016/j.egypro.2015.07.555>.
- [2] M. Naumann, *Techno-economic Evaluation of Stationary Battery Energy Storage Systems with Special Consideration of Aging*, Dissertation, Technische Universität München, München, 2018.
- [3] Technical University of Munich, Web portal of the energy neighbor (accessed: 2019-08-20), <https://www.mse.tum.de/en/eebatt/energy-neighbor/>.
- [4] C.N. Truong, M. Schimpe, M. Naumann, A. Jossen, H.C. Hesse, Impact of sub-components on the overall performance of stationary battery systems: insights on the prototype energy neighbor, in: *International ETG Congress 2017, ETG-Fachbericht*, VDE Verlag, Berlin and Offenbach, 2017, pp. 1–6.
- [5] Technical University of Munich, EEBatt - interdisciplinary energy storage research project (accessed: 2019-08-20), <https://www.mse.tum.de/eebatt/>.
- [6] A. Barré, B. Deguilhem, S. Grolleau, M. Gérard, F. Suard, D. Riu, A review on lithium-ion battery ageing mechanisms and estimations for automotive applications, *J. Power Sources* 241 (2013) 680–689, <https://doi.org/10.1016/j.jpowsour.2013.05.040>.
- [7] D. Li, D.L. Danilov, L. Gao, Y. Yang, P.H.L. Notten, Degradation mechanisms of the graphite electrode in c6/lifepo 4 batteries unraveled by a non-destructive approach, *J. Electrochem. Soc.* 163 (14) (2016) A3016–A3021, <https://doi.org/10.1149/2.0821614jes>.
- [8] S.F. Schuster, T. Bach, E. Fleder, J. Müller, M. Brand, G. Sextl, A. Jossen, Nonlinear aging characteristics of lithium-ion cells under different operational conditions, *Journal of Energy Storage* 1 (2015) 44–53, <https://doi.org/10.1016/j.est.2015.05.003>.
- [9] M. Lepiorz, *Betriebsbedingte Alterung von Lithium-Ionen Batterien in stationären und mobilen Anwendungen*, Dissertation, first ed., Ingenieurwissenschaften, Verlag Dr. Hut, München, 2016.
- [10] J. de Hoog, J.-M. Timmermans, D. Ioan-Stroe, M. Swierczynski, J. Jaguemont, S. Goutam, N. Omar, J. van Mierlo, P. van den Bossche, Combined cycling and calendar capacity fade modeling of a nickel-manganese-cobalt oxide cell with real-life profile validation, *Appl. Energy* 200 (2017) 47–61, <https://doi.org/10.1016/j.apenergy.2017.05.018>.
- [11] J. Schmalstieg, S. Käbitz, M. Ecker, D.U. Sauer, A holistic aging model for li (nimnco)o2 based 18650 lithium-ion batteries, *J. Power Sources* 257 (2014) 325–334, <https://doi.org/10.1016/j.jpowsour.2014.02.012>.
- [12] E. Prada, D. Di Domenico, Y. Creff, J. Bernard, V. Sauvant-Moynot, F. Huet, A simplified electrochemical and thermal aging model of lifepo4-graphite li-ion batteries: power and capacity fade simulations, *J. Electrochem. Soc.* 160 (4) (2013) A616–A628, <https://doi.org/10.1149/2.053304jes>.
- [13] E. Sarasketa-Zabala, I. Gandiaga, E. Martinez-Laserna, L.M. Rodriguez-Martinez, I. Villarreal, Cycle ageing analysis of a lifepo4/graphite cell with dynamic model validations: towards realistic lifetime predictions, *J. Power Sources* 275 (2015) 573–587, <https://doi.org/10.1016/j.jpowsour.2014.10.153>.
- [14] E. Sarasketa-Zabala, E. Martinez-Laserna, M. Berceibar, I. Gandiaga, L. M. Rodriguez-Martinez, I. Villarreal, Realistic lifetime prediction approach for li-ion batteries, *Appl. Energy* 162 (2016) 839–852, <https://doi.org/10.1016/j.apenergy.2015.10.115>.
- [15] I. Bloom, B. Cole, J. Sohn, S. Jones, E. Polzin, V. Battaglia, G. Henriksen, C. Motloch, R. Richardson, T. Unkelhaeuser, D. Ingersoll, H. Case, An accelerated calendar and cycle life study of li-ion cells, *J. Power Sources* 101 (2) (2001) 238–247, [https://doi.org/10.1016/S0378-7753\(01\)00783-2](https://doi.org/10.1016/S0378-7753(01)00783-2).
- [16] S. Käbitz, J.B. Gerschler, M. Ecker, Y. Yurdagel, B. Emmermacher, D. Andr, T. Mitsch, D.U. Sauer, Cycle and calendar life study of a graphite—lini1/3mn1/3co1/3o2 li-ion high energy system. part a: full cell characterization, *J. Power Sources* 239 (2013) 572–583, <https://doi.org/10.1016/j.jpowsour.2013.03.045>.
- [17] M. Lewerenz, J. Münnix, J. Schmalstieg, S. Käbitz, M. Knips, D.U. Sauer, Systematic aging of commercial lifepo4—graphite cylindrical cells including a theory explaining rise of capacity during aging, *J. Power Sources* 345 (2017) 254–263, <https://doi.org/10.1016/j.jpowsour.2017.01.133>.
- [18] M. Swierczynski, D.-I. Stroe, A.-I. Stan, R. Teodorescu, S.K. Kaer, Lifetime estimation of the nanophosphate lifepo4/c battery chemistry used in fully electric vehicles, *IEEE Trans. Ind. Appl.* 51 (4) (2015) 3453–3461, <https://doi.org/10.1109/TIA.2015.2405500>.
- [19] M. Petit, E. Prada, V. Sauvant-Moynot, Development of an empirical aging model for li-ion batteries and application to assess the impact of vehicle-to-grid strategies on battery lifetime, *Appl. Energy* 172 (2016) 398–407, <https://doi.org/10.1016/j.apenergy.2016.03.119>.
- [20] J. Wang, P. Liu, J. Hicks-Garner, E. Sherman, S. Soukiazian, M. Verbrugge, H. Tataria, J. Musser, P. Finamore, Cycle-life model for graphite-lifepo4 cells, *J. Power Sources* 196 (8) (2011) 3942–3948, <https://doi.org/10.1016/j.jpowsour.2010.11.134>.
- [21] J. Wang, J. Purewal, P. Liu, J. Hicks-Garner, S. Soukiazian, E. Sherman, A. Sorenson, L. Vu, H. Tataria, M.W. Verbrugge, Degradation of lithium ion batteries employing graphite negatives and nickel—cobalt—manganese oxide + spinel manganese oxide positives: Part 1, aging mechanisms and life estimation, *J. Power Sources* 269 (2014) 937–948, <https://doi.org/10.1016/j.jpowsour.2014.07.030>.
- [22] C. Delacourt, M. Safari, Life simulation of a graphite/lifepo4 cell under cycling and storage, *J. Electrochem. Soc.* 159 (8) (2012) A1283–A1291, <https://doi.org/10.1149/2.049208jes>.
- [23] H. Ekström, G. Lindbergh, A model for predicting capacity fade due to sei formation in a commercial graphite/lifepo4 cell, *J. Electrochem. Soc.* 162 (6) (2015) A1003–A1007, <https://doi.org/10.1149/2.0641506jes>.
- [24] K.L. Gering, Novel method for evaluation and prediction of capacity loss metrics in li-ion electrochemical cells, *Electrochim. Acta* 228 (2017) 636–651, <https://doi.org/10.1016/j.electacta.2017.01.052>.
- [25] M. Safari, C. Delacourt, Simulation-based analysis of aging phenomena in a commercial graphite/lifepo4 cell, *J. Electrochem. Soc.* 158 (12) (2011) A1436, <https://doi.org/10.1149/2.103112jes>.
- [26] K. Rumpf, M. Naumann, A. Jossen, Experimental investigation of parametric cell-to-cell variation and correlation based on 1100 commercial lithium-ion cells, *Journal of Energy Storage* 14 (2017) 224–243, <https://doi.org/10.1016/j.est.2017.09.010>.
- [27] J. Wilhelm, S. Seidlmayer, P. Keil, J. Schuster, A. Kriele, R. Gilles, A. Jossen, Cycling capacity recovery effect: a coulombic efficiency and post-mortem study, *J. Power Sources* 365 (2017) 327–338, <https://doi.org/10.1016/j.jpowsour.2017.08.090>.
- [28] Energie-Forschungszentrum Niedersachsen, H.-P. Beck, H. Bart, B. Bayer, J. Klee Barillas, M. Danzer, M. Dennenmoser, M. Naumann, Potentielle elektrochemischer Speicher in elektrischen Netzen in Konkurrenz zu anderen Technologien und Systemlösungen (ESPEN): Abschlussbericht, TIB - Technische Informationsbibliothek Universitätsbibliothek Hannover, Göttingen, 2016, <https://doi.org/10.2314/GBV:869930222>.
- [29] M. Naumann, C.N. Truong, M. Schimpe, D. Kucevic, A. Jossen, H.C. Hesse, Simses: software for techno-economic simulation of stationary energy storage systems, in: *International ETG Congress*, 2017, pp. 1–6.